A LARGE STELLAR EVOLUTION DATABASE FOR POPULATION SYNTHESIS STUDIES. VI. WHITE DWARF COOLING SEQUENCES

M. SALARIS[1], S. CASSISI[2], A. PIETRINFERNI[2], P. M. KOWALSKI[3], AND J. ISERN[4,5]
[1] Astrophysics Research Institute, Liverpool John Moores University, 12 Quays House, Birkenhead, CH41 1LD, UK; ms@astro.livjm.ac.uk
[2] INAF-Osservatorio Astronomico di Collurania, via M. Maggini, 64100 Teramo, Italy; cassisi@oa-teramo.inaf.it, adriano@oa-teramo.inaf.it
[3] Helmholtz-Centre Potsdam-GFZ German Research Centre for Geosciences, Section 3.3, D-14473, Potsdam, Germany
[4] Institut de Ciéncies de l'Espai (CSIC), Facultat de Ciéncies, Campus UAB, 08193 Bellaterra, Spain
[5] Institut d'Estudis Espacials de Catalunya, c/Gran Capita 2-4, Edif. Nexus 104, 08034 Barcelona, Spain

ABSTRACT

We present a new set of cooling models and isochrones for both H- and He-atmosphere white dwarfs (WDs), incorporating accurate boundary conditions from detailed model atmosphere calculations, and carbon–oxygen chemical abundance profiles based on updated stellar evolution calculations from the BaSTI stellar evolution archive—a theoretical data center for the Virtual Observatory. We discuss and quantify the uncertainties in the cooling times predicted by the models, arising from the treatment of mixing during the central H- and He-burning phases, the number of thermal pulses experienced by the progenitors, progenitor metallicity, and the $^{12}C(\alpha, \gamma)^{16}O$ reaction rate. The largest sources of uncertainty turn out to be related to the treatment of convection during the last stages of the progenitor central He-burning phase and the $^{12}C(\alpha, \gamma)^{16}O$ reaction rate. We compare our new models to previous calculations performed with the same stellar evolution code, and discuss their application to the estimate of the age of the solar neighborhood and the interpretation of the observed number ratios between H- and He-atmosphere WDs. The new WD sequences and an extensive set of WD isochrones that cover a large range of ages and progenitor metallicities are made publicly available at the official BaSTI Web site.

Key words: Galaxy: disk – galaxies: stellar content – stars: evolution – stars: interiors – white dwarfs

Online-only material: color figures

1. INTRODUCTION

The interpretation of photometric and spectroscopic observations of stellar populations relies on the use of grids of stellar models and isochrones that have to cover a wide range of initial chemical compositions, stellar masses, and evolutionary phases. The BaSTI (a Bag of Stellar Tracks and Isochrones) project[6] started in 2004 has delivered, to date, a homogeneous database of stellar evolution models, isochrones and integrated spectra for single-age, single-metallicity populations, encompassing a large chemical composition range appropriate for stellar populations harbored in star clusters and galaxies of various morphological types (Pietrinferni et al. 2004, 2006, 2009; Cordier et al. 2007; Percival et al. 2009). Results from BaSTI projects have been used by a large number of authors to address very diverse astrophysical problems such as, among others, fitting eclipsing binary systems in the mass–radius plane, determining the ages of star clusters from their color–magnitude diagrams (CMDs), or comparing integrated colors of elliptical galaxies with theoretical predictions.

BaSTI models and isochrones in their present form cover all relevant evolutionary phases until either the end of the thermal pulse regime along the asymptotic giant branch (AGB), or central carbon ignition for masses without electron degenerate carbon–oxygen (CO) cores. In this paper, we extend the evolutionary phase coverage of our database to include cooling models of CO-core white dwarf (WDs), the final evolutionary phase of stars with initial masses smaller than about 6–7 $M_\odot$.

During the last two decades observations and theory have improved to a level that has finally made possible to employ WDs for determining the ages of the stellar populations in the solar neighborhood (e.g., Winget et al. 1987; Garcia-Berro et al. 1988b; Wood 1992; Oswalt et al. 1996), and in the nearest open (e.g., Richer et al. 1998; von Hippel 2005; Bedin et al. 2008, 2010) and globular (e.g., Hansen et al. 2004, 2007; Bedin et al. 2009) clusters. Methods to determine stellar population ages from their WD cooling sequences are usually based on the comparison of either the observed WD luminosity function (LF—star counts as a function of magnitude, e.g., Winget et al. 1987; Bedin et al. 2010) or the actual bidimensional WD distribution in the CMD, with their theoretical counterparts (see, e.g., Hansen et al. 2007). Both techniques rely on an extensive use of grids of WD cooling sequences.

The sets of WD models largely employed in the more recent investigations on the age of WDs in Galactic stellar populations are those by Hansen (1999, hereafter H99) and Salaris et al. (2000, hereafter S00), computed with completely independent evolutionary codes and largely independent input physics. Additional recent large sets of WD evolutionary cooling models can be found in Althaus & Benvenuto (1998; and later updates from the same group, which has also produced extensive libraries of He-core WD models, presented in Serenelli et al. 2002, Althaus et al. 2009, and Fontaine et al. 2001). The new grid of cooling models, we present here to extend the evolutionary phase coverage of BaSTI, is an update of the results by S00. We include a complete set of both H- and He-atmosphere WD models (and isochrones, for a range of progenitor initial chemical compositions) that take advantage of the updated CO stratifications obtained from BaSTI AGB models, and employ boundary conditions from new sets of calculations of WD H and He atmospheres. Along with the presentation of our new models, we will discuss critically how WD cooling times are affected by the progenitor metallicity, uncertainties on the current estimate of the $^{12}C(\alpha, \gamma)^{16}O$ reaction rate and treatment of convection

---

[6] Official Web site at http://www.oa-teramo.inaf.it/BASTI.

during the progenitor evolution. A similar analysis (albeit with several differences in the details) can be found in Prada-Moroni & Straniero (2002), without taking into account CO phase separation upon crystallization in the WD cooling models.

The paper is structured as follows. Section 2 presents briefly the updates in the input physics compared to S00, and discusses critically our choices for the core chemical stratifications. Section 3 analyzes the main properties of the cooling models and WD isochrones, and shows comparisons with S00 calculations and an example of application to study WDs in the solar neighborhood. A summary follows in Section 4.

2. INPUT PHYSICS, CORE, AND ENVELOPE STRATIFICATION

The cooling code employed in our calculations is the same described in S00, and the reader is referred to that paper for more details about the model input physics. The only differences compared to S00 calculations involve boundary conditions, the core and envelope chemical compositions, and will be described below.

We provide WD cooling models for masses equal to 0.54, 0.55, 0.61, 0.68, 0.77, 0.87, and $1.0 M_\odot$, as in S00, plus WD isochrones, both neglecting and including the release of gravitational energy associated with the phase separation of the CO mixture upon crystallization (e.g., Stevenson 1977; Mochkovitch 1983; Garcia-Berro et al. 1988a; Segretain et al. 1994; Montgomery et al. 1999; Isern et al. 2000, and references therein). The effect of phase separation is calculated as in S00.

The range of WD masses presented here ensures a good coverage of the full spectrum of WD masses derived from semiempirical progenitor–WD (initial–final) mass relationships (see, e.g., Salaris et al. 2009).

Similar to S00, for each WD mass an initial model was converged at $\log(L/L_\odot) \sim 1.0$–1.5 by considering a reference CO stratification in the core, and a reference thickness and chemical composition of the envelope layers.

2.1. Envelope Chemical Stratification

We have computed WD models considering both pure H and pure He atmospheres. The H-atmosphere WD models have "thick" H layers, as in H99 and S00 (and the H-atmosphere models by Fontaine et al. 2001); the envelope consists of an H layer with mass fraction $q_H = 10^{-4} M_{WD}$ on top of an He layer of mass $q_{He} = 10^{-2} M_{WD}$. The He-atmosphere WD models have an He envelope with mass fraction $q_{He} = 10^{-3.5} M_{WD}$, as in H99. With these choices for q_H and q_{He}, the surface convective regions that develop during the cooling process are not able to cross the H–He interface in H-atmosphere models, or the He–CO interface in He-atmosphere models.

Rosseland low-temperature ($T < 10,000$ K) opacities by Alexander et al. (1997) for a pure He composition are employed in the envelope calculations of He-atmospheres models, while the Saumon & Jacobson (1999) low-temperature opacities are employed for the hydrogen envelopes, as in S00. At higher temperatures, we employed the OPAL (Iglesias & Rogers 1993) radiative opacities for the appropriate chemical composition. As mentioned before, our envelopes have zero metal content, even though progenitor models have non-zero initial metallicity. Given the high efficiency of atomic diffusion at the very beginning of the cooling sequence (e.g., Koester 2009) all metals in the WD envelopes have settled above the core boundary. To have an approximate estimate of this effect on our

H-atmosphere cooling models, we have computed the evolution of a $0.61 M_\odot$ model (for the reference CO stratification discussed in Section 2.3) keeping the hydrogen layers metal free, but considering a metal mass fraction $Z = 0.0198$—the initial solar metal abundance in the BaSTI solar model (Pietrinferni et al. 2004)—distributed uniformly throughout the underlying He envelope. Comparison of the cooling times with the $Z = 0$ case in the whole envelope shows differences by typically less than 1%. In the case of the He-atmosphere cooling models, a rough estimate of the same effect has been derived by calculating the evolution of a $0.61 M_\odot$ model with metals (initial metallicity $Z = 0.0198$) redistributed uniformly in the deeper envelope layers where the pressure is more than 6 orders of magnitude higher than the photosphere. This means that the photosphere and outer envelope are still metal free, as in the reference case. We have found differences in the cooling times by at most $\sim2\%$, compared to the metal free case.

As a final comment, we remark that the thickness of the envelope layers in our models is the same for the whole range of WD masses. Also any possible dependence on the progenitor metallicity will be disregarded. Results from evolutionary models that follow the evolution throughout the AGB phase until the WD cooling sequence (see, e.g., Iben & MacDonald 1986) show a dependence of q_H and q_{He} on progenitor mass and initial chemical composition, but the uncertainties in the theoretical predictions of the WD envelope thickness are still large, i.e., they depend crucially on the precise description of the mass loss events during the Thermal Pulse (TP) phase. Calculations with constant thickness of the envelope layers provide a useful reference baseline grid of WD models that allow to disentangle in a more direct way the effect of the existing uncertainties related to core and envelope physical and chemical properties.

For our choice of q_H and q_{He} and the starting luminosities of our calculations, H-burning at the bottom of the H envelope is negligible in all but the more massive models and does not affect cooling times and the value of q_H. For the more massive models, we have estimated with test calculations that the effect of H-burning on the cooling times amounts to a few percent. In order to keep q_H at a strictly constant value for the whole model grid, we have inhibited nuclear burning in all calculations discussed in this paper.

2.2. Boundary Conditions

The surface boundary conditions needed to integrate the stellar structure (P and T at $\tau = 100$, where the diffusion approximation is valid and one can safely start to integrate the full set of stellar structure equations using Rosseland mean opacities) were obtained for $T_{eff} < 10,000$ K from detailed non-gray model atmospheres. These include the latest physical improvements in the calculation of the chemistry, opacity, radiative transfer, and equation of state of dense hydrogen and helium in WD atmospheres (Kowalski & Saumon 2004, 2006; Kowalski 2006a, 2006b, Kowalski et al. 2007). At higher T_{eff}, the boundary conditions have been calculated by integrating a gray $T(\tau)$ relationship. As discussed in S00 (see also H99) in this temperature regime a gray $T(\tau)$ integration is a suitable choice.

Figure 1 compares the luminosity–central temperature (L–T_c) relationships for two representative $0.61 M_\odot$ and $0.87 M_\odot$ cooling models, with both H and He atmospheres. As discussed in S00 and H99, the L–T_c relationship at fixed M_{WD} depends only on the properties of the non-degenerate envelope and atmosphere, and is independent of the CO stratification and the
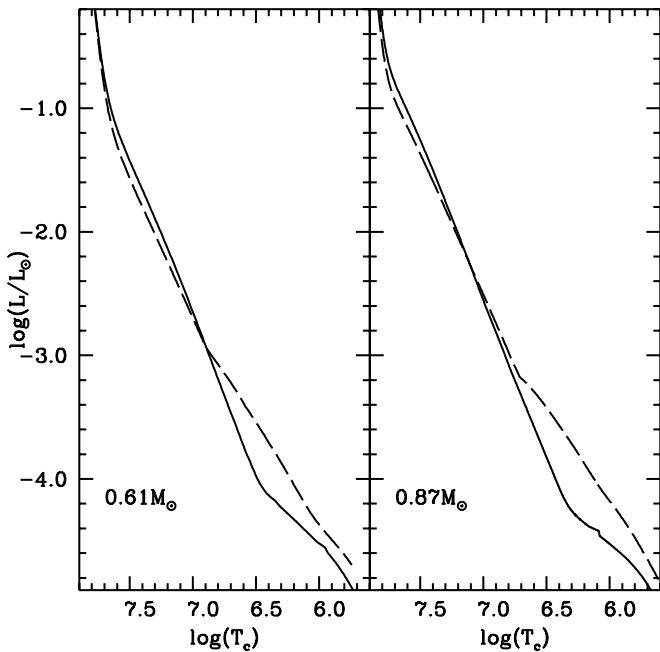
Figure 1. L–T_c relationships for our 0.61 and 0.87 $M_\odot$ WD models (without phase separation). Solid lines denote H-atmosphere models, dashed lines He-atmosphere ones.

Figure 2. Reference oxygen stratification (in mass fraction) for our WD models. Labels denote, in order of increasing number, the abundances for the 0.54, 0.55, 0.61, 0.68, 0.77, 0.87, and 1.0 $M_\odot$ models, respectively.

(A color version of this figure is available in the online journal.)

treatment of crystallization (we display in the figure the results without phase separation). In the case of the 0.61 $M_\odot$ model, the He envelope/atmosphere has a higher opacity (the same T_c is reached at lower luminosities) between $\log(L/L_\odot) \sim -1$ and ~ -3.0. Below $\log(L/L_\odot) \sim -3.0$ the two relationships start to diverge considerably (see also Figure 8 in H00), the He envelope external layers becoming sizably less opaque when the atmospheres become neutral (H99). At lower luminosities they tend to move back close to each other. As for the 0.87 $M_\odot$ model, the behavior is very similar. The luminosity at which the He envelope becomes less opaque is shifted to slightly higher values, compared to the 0.61 $M_\odot$ model.

As a test, we have also compared our new H envelope L–T_c relationship with the S00 one for the same 0.61 $M_\odot$ mass, and did not find any difference between the two models.

2.3. CO Profiles

The choice of the CO stratification is extremely important, given that the rate of cooling is determined, among other factors, by the ionic specific heat, which depends on the relative proportions of carbon and oxygen. The additional source of energy provided by the crystallization process is also greatly affected by the CO profile (see, e.g., Salaris et al. 1997).

Our adopted reference CO stratifications have been obtained from the grid of BaSTI scaled solar stellar evolution models. More in detail, we employed the sets of models with the initial solar metal abundance ($Z = 0.0198$) that include convective core overshooting during the main sequence, for it appears to be necessary to reproduce the CMD and star counts in young and intermediate age star clusters (see, e.g., the discussion in Pietrinferni et al. 2004, and references therein). Core mixing during central He-burning is treated by including semiconvection according to the method described by Castellani et al. (1985). The breathing pulses occurring during the last portion of core He-burning have been inhibited following the method by Caputo et al. (1989). The reader is referred to, e.g., Cassisi et al. (2001)
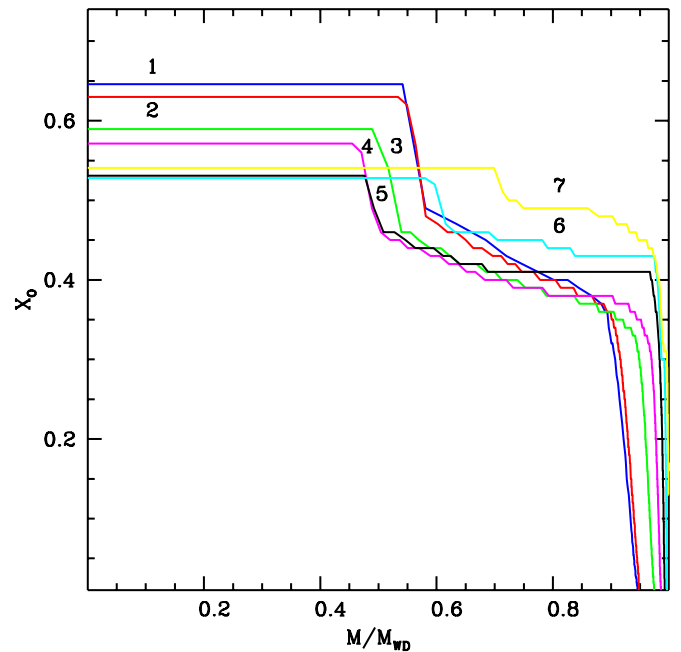
and Cassisi et al. (2003) for a discussion about breathing pulses and observational constraints on their efficiency.

For a given value of $M_{\rm WD}$, we have taken the core stratification at the first thermal pulse from the progenitor model whose mass internal to the He–H discontinuity is equal to $M_{\rm WD}$. If for some of our selected WD masses there is no model in the original BaSTI grid that displays the appropriate core mass at the first thermal pulse, we have performed additional calculations. All our reference chemical profiles are displayed in Figure 2, and are kept fixed in all WD isochrones, we will make available in BaSTI, that span a large range of progenitor metallicities. This means that, when we compute WD isochrones for a stellar population of a given initial composition, only as far as the WD initial chemical stratification is concerned, we are neglecting the effect of the progenitor metallicity and we are assuming an initial–final mass relationship (IFMR) given by the core masses at the first thermal pulse of models including core overshooting during the main sequence. We notice here that with our reference CO stratifications, the onset of the convective coupling with electron degenerate layers—a process discussed in detail by Fontaine et al. (2001)—overlaps in time with the crystallization of the CO core, for the full range of WD masses.

In the following, we will evaluate the impact of these assumptions about the CO profile on the cooling times of a 0.61 $M_\odot$ WD model (we performed the same analysis for a 1.0 $M_\odot$ model, and obtained very similar results) in comparison with the effect of two major intrinsic uncertainties in the modeling of the central He-burning phase, namely, the method for breathing pulse suppression and the $^{12}{\rm C}(\alpha, \gamma)^{16}{\rm O}$ reaction rate. To do so, we take advantage of additional calculations for the progenitor evolutions performed for this work.

2.3.1. Main Sequence Core Overshooting

Figure 3 displays several O-abundance profiles (in mass fraction) for a 0.61 $M_\odot$ WD model, calculated under different
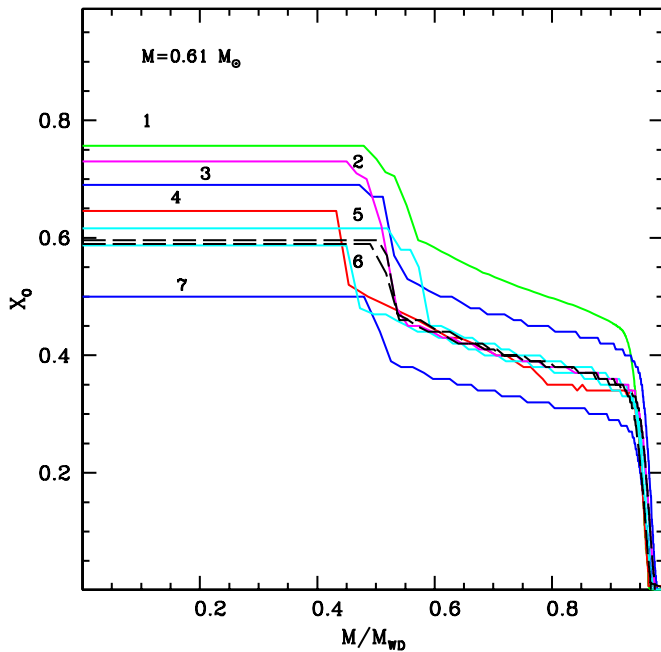
Figure 3. Several different oxygen stratification (in mass fraction) tested on a 0.61 $M_\odot$ WD model. See the text for details.

(A color version of this figure is available in the online journal.)

assumptions, all taken after the rehomogeneization by Rayleigh–Taylor instability discussed in Salaris et al. (1997). The two dashed lines correspond to progenitor models at the first thermal pulse computed with (our reference choice—the profile with a very slightly higher central oxygen abundance) and without core overshooting on the main sequence. The two stratifications are almost identical, in spite of the fact that the progenitor mass is ~3.0 $M_\odot$ for the model with main sequence core overshooting, and ~3.5 $M_\odot$ for the model without overshooting. The reason is that the CO stratification at the start of the thermal pulse phase is determined by the value of the He-core mass at the onset of the He-burning—that is approximately the same in both progenitors—not by the total mass. As a general property of the final CO profiles, the inner part of the core, with a constant abundance of oxygen (see Salaris et al. 1997 for more details on this issue) is determined by the maximum extension of the central He-burning convective region. Beyond this region, the oxygen profile is built when the thick He-burning shell moves toward the surface. During this phase, gravitational contraction increases temperature and density of the shell, and since the ratio between the $^{12}C(\alpha, \gamma)^{16}O$ and 3α reaction rates is lower for larger temperatures (see, e.g., Figure 1 in Mazzitelli & D'Antona 1987), the oxygen mass fraction steadily decreases in the external part of the CO core.

2.3.2. Progenitor Metallicity and IFMR

The profiles labeled as 5 and 6 in Figure 3 show the case of progenitors with metallicity equal to $Z = 0.002$ and $Z = 0.04$ (with main sequence core overshooting, as for all other calculations discussed below), respectively. The mass of the progenitor with $Z = 0.002$ is ~1.0 $M_\odot$ lower than our reference case, whereas it is approximately the same for the $Z = 0.04$ model. The central value of the oxygen abundance is almost the same (within at most ~0.02 in mass fraction) as the reference choice. The only major change is the mass extension of the inner region with the highest oxygen abundance.

Profile number 4 shows the oxygen abundance profile obtained using a different IFMR from the reference case. The progenitor metallicity is $Z = 0.0198$ as in the reference case, but we started with a mass ~1.0 $M_\odot$ lower (~2 $M_\odot$ instead of ~3 $M_\odot$) and let the model evolve through several thermal pulses until the core reached 0.61 $M_\odot$. This choice for the progenitor is roughly consistent with the semiempirical IFMR determined by Salaris et al. (2009).

The central oxygen abundance is larger (by about 5%) than the reference case, because of the smaller initial progenitor mass, that produces a higher central O abundance. The extension of the central region with the highest oxygen content is smaller, reflecting the reduced size of both the convective inner regions, and the overall He core during the central He-burning phase.

2.3.3. Breathing Pulse Suppression and $^{12}C(\alpha, \gamma)^{16}O$ Reaction Rate

Profiles labeled as 2, 3, and 7 display the effect of two major intrinsic uncertainties in the derivation of evolutionary CO profiles for WDs. Profile number 2 shows the result at the first pulse for a progenitor with $Z = 0.0198$, but the breathing pulses suppressed following a different method devised by Dorman & Rood (1993; see, e.g., Cassisi et al. 2003 for more details on this issue). The major effect is on the central oxygen mass fraction that increases by ~15% (see also Straniero et al. 2003 for a similar test).

Profiles 3 and 7 show the abundances (for progenitor metallicity $Z = 0.0198$) at the first pulse using the lower and upper limits of our adopted $^{12}C(\alpha, \gamma)^{16}O$ reaction rate, from Kunz et al. (2002). It is important to notice how more recent estimates of the astrophysical S-factor for this reaction (Katsuma 2008; Dufour & Descouvemont 2008) provide values roughly within the limits given by Kunz et al. (2002).

The progenitor mass is essentially the same as our reference case, but the final profiles are obviously affected by the different rates. We also displayed, for comparison, the oxygen profile (profile 1) used by S00 and taken from Salaris et al. (1997) progenitor calculations. The main reason for the sizable differences with our reference choice is that Salaris et al. (1997) adopted the $^{12}C(\alpha, \gamma)^{16}O$ rate by Caughlan et al. (1985). The more recent calculations by Kunz et al. (2002) give a lower reaction rate that causes an overall smaller oxygen abundance at the same value of the core mass.

2.3.4. Discussion

It is clear from Figure 3 that the uncertainties related to the $^{12}C(\alpha, \gamma)^{16}O$ rate and the breathing pulse suppression have on the whole the largest influence on the WD chemical stratification. Figure 4 compares the cooling times of several 0.61 $M_\odot$ H-atmosphere WD models (including the effect of phase separation) computed employing the profiles discussed above. We display the fractional difference between the cooling ages of a model with our reference profile and models with each one of the other choices shown in Figure 3. During the precrystallization phase ($\log(L/L_\odot)$ above ~-3.6 and ages below ~2.0 Gyr for the reference model) cooling times differ overall by less than ±2%, the largest variations being caused by the $^{12}C(\alpha, \gamma)^{16}O$ rate and breathing pulse suppression uncertainties. As a general rule, during this phase the models with a higher oxygen abundance tend to cool faster, as expected. Below $\log(L/L_\odot) \sim -4.2$ (ages above ~5 Gyr for the reference model) when the crystallization of the CO core is almost completed, $^{12}C(\alpha, \gamma)^{16}O$ and breathing pulses are again the major sources
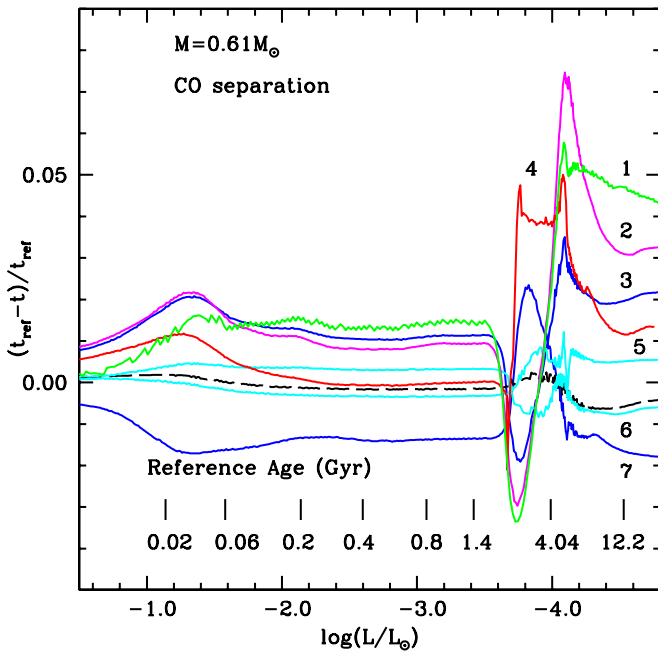
Figure 4. Fractional difference between the cooling ages of models with our reference profile (t_{ref}) and models with the alternative choices displayed in Figure 3 (t). Labels correspond to the profiles displayed in Figure 3. The dashed line denotes the difference with respect to the stratification obtained with the same assumptions of our reference choice, but without considering main sequence core overshooting for the progenitor evolution. Selected ages for the model with the reference O-profile are also displayed.

(A color version of this figure is available in the online journal.)

Figure 5. Cooling times as a function of the surface bolometric luminosity for our complete set of H-atmosphere models (including crystallization but without phase separation). At a reference $\log(L/L_\odot) = -3.5$, from bottom to top, the different lines denote the 0.54, 0.55, 0.61, 0.68, 0.77, 0.87, and 1.0 $M_\odot$ model, respectively.

of uncertainty, at the level of 2%–3%. At luminosities and ages intermediate between these two regimes the situation is more complex, because the exact luminosity of the onset of crystallization—and the associated energy release due to latent heat and phase separation—varies with changing abundance profiles. In general, the higher the central oxygen abundance the earlier the onset of crystallization. This explains the narrow luminosity range (around $\log(L/L_\odot) \sim -3.6$) where cooling times are generally longer for models with higher central oxygen. During the crystallization process the exact values of the cooling times depend on the detailed shape of the CO profile. As a result, at luminosities between $\log(L/L_\odot) \sim -3.6$ and $\log(L/L_\odot) \sim -4.0$, the model with a lower mass progenitor that mimics a realistic IFMR displays the longest cooling times. Differences with our reference choice are still below 5%.

When the effect of phase separation upon crystallization is neglected, the qualitative behavior of the age differences is exactly the same discussed before, but quantitatively the fractional differences are smaller, always within $\sim\pm3\%$, at all luminosities/ages.

To summarize, Figure 4 shows that selecting CO profiles from progenitor models at the first thermal pulse, and discarding metallicity effects on the progenitor evolution, does not introduce major uncertainties in the cooling times of models at fixed M_{WD}. On the whole, a larger effect—still within at most 7% or 3% when phase separation is neglected—is caused by the treatment of convection in the late stages of the progenitor central He-burning phase, and the uncertainty on the $^{12}C(\alpha, \gamma)^{16}O$ rate. Only during the first stages of crystallization the choice of the IFMR has the largest impact on the cooling timescales, but the effect is within 5%, and at most 3% when phase separation is neglected.
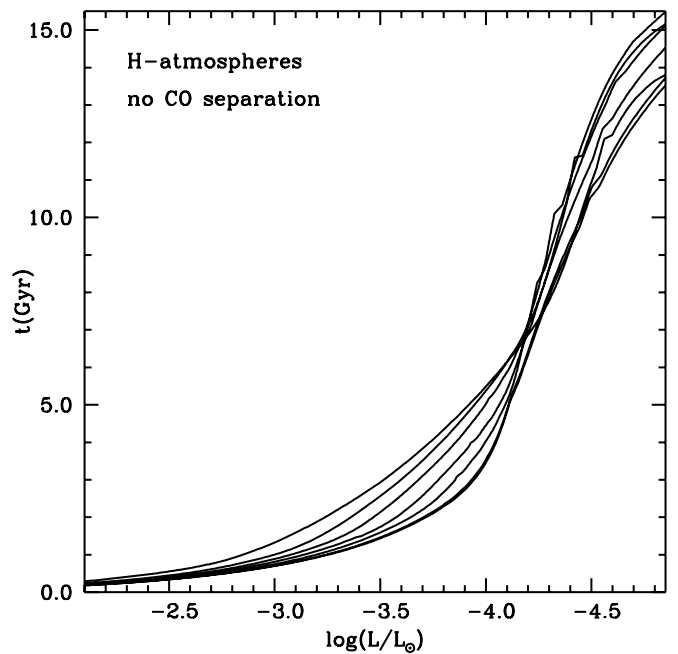
It is also important to mention briefly the crucial role played by the thickness of the H envelope. A decrease of q_H from $q_H = 10^{-4}\, M_{WD}$ to $q_H = 10^{-5}\, M_{WD}$, keeping the core chemical composition unchanged, speeds up the cooling of the models, causing a maximum age difference of $\sim7\%$ at ages above ~4 Gyr, in the case of both including and neglecting the effect of phase separation.

3. COOLING SEQUENCES AND ISOCHRONES

Our new sets of WD cooling models have been computed with the choices for the envelope and core stratifications discussed in detail in the previous section. The cooling times as a function of luminosity for the full set of WD masses are shown in Figure 5, in the case of models with H atmospheres and no CO phase separation upon crystallization. The fractional age difference $\Delta t/t$ with respect to He-atmosphere WD calculations (no phase separation included) for two selected WD masses is shown in Figure 6. At luminosities above $\log(L/L_\odot) \sim -4.0$ (the exact value depending on M_{WD}) He-atmosphere models predict longer cooling times (up to $\sim30\%$–50%) first due to the higher opacity of their envelopes in this luminosity range (see Figure 1) and then, when their envelopes become less opaque, due to an earlier onset of crystallization and earlier latent heat release. Below $\log(L/L_\odot) \sim -4.0$ the H-atmosphere WDs show progressively longer cooling times, due to the much higher opacity of their envelopes, and $\Delta t/t$ reaches values up to 50% at $\log(L/L_\odot) \sim -4.6$ to -4.7, the faintest luminosities of our He-atmosphere calculations.

The total time delay t_d caused by the inclusion of CO phase separation is displayed in Figure 7 for the full set of H- and He-atmosphere WD calculations. As in the case of S00 calculations, for H-atmosphere WD models t_d increases with mass, has a maximum at $M_{WD} = 0.77\, M_\odot$, and then decreases. Because of the different CO profile, with the C/O ratio typically closer to
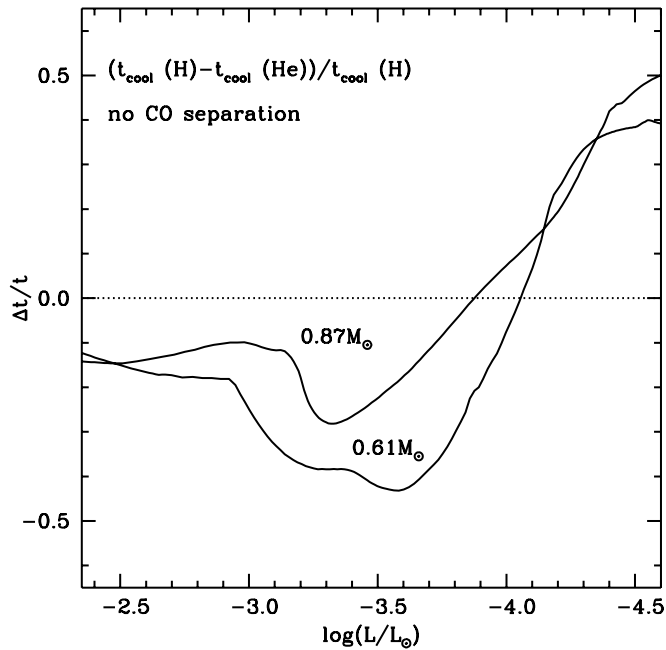
Figure 6. Fractional difference between the cooling times of H- and He-atmosphere WD models (phase separation not included) with masses equal to 0.61 and 0.87 $M_\odot$, respectively.
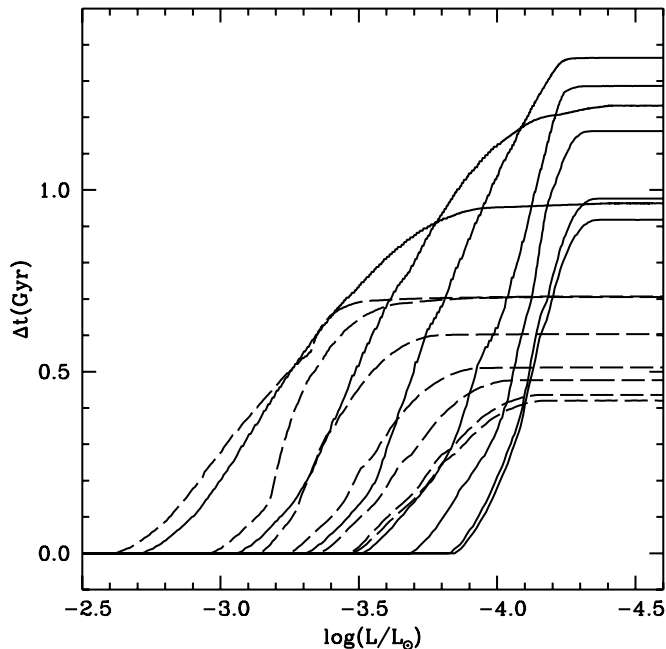

Figure 7. Time delay Δt caused by the inclusion of CO phase separation upon crystallization, as a function of the WD luminosity. From right to left, the different lines denote the 0.54, 0.55, 0.61, 0.68, 0.77, 0.87, and 1.0 $M_\odot$ model, respectively. Dashed (solid) lines represent He- (H-) atmosphere WD models. The total time delay t_d corresponds to the final, constant value of Δt, when crystallization is completed.

1 in the central regions, our new H-atmosphere models display on average ∼100 Myr larger t_d at fixed M_{WD} compared to the S00 results. In the case of He-atmosphere WD calculations t_d increases with mass and reaches a maximum for the 0.87 and 1.0 $M_\odot$ models. In quantitative terms t_d is roughly a factor of 2 larger for the H-atmosphere models, due essentially to the higher opacity of their envelopes when crystallization sets in.

Figure 8 displays the mass–radius relationship for both H- and He-atmosphere WD models, taken at three different
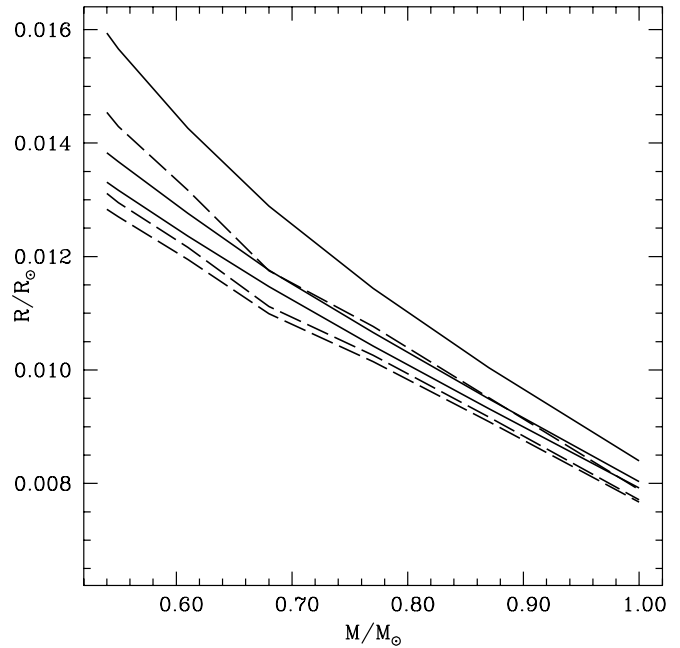

Figure 8. Mass–radius relationship (in solar units) for our H- (solid lines) and He-atmosphere (dashed lines) models, taken at T_{eff} equal to (moving from top to bottom) 30,000, 10,000, and 5000 K, respectively.

effective temperatures along the cooling sequences. As already investigated by, e.g., Bergeron et al. (1992) the radii of He-atmosphere WDs of a given mass turn out to be systematically smaller than the H-atmosphere case. For our models, typical differences at $T_{eff} = 30,000$ K are of ∼9% for $M_{WD} = 0.54\,M_\odot$, decreasing down to ∼6% for $M_{WD} = 1.0\,M_\odot$. When T_{eff} has decreased to 5000 K the differences are ∼4% for $M_{WD} = 0.54\,M_\odot$ and ∼3% for $M_{WD} = 1.0\,M_\odot$

Starting from the cooling models, we have computed WD isochrones, i.e., the CMD of WDs born from a single-age, single-metallicity population. Isochrones are a a fundamental tool for stellar population dating, and are routinely used to study the cooling sequences of WDs in star clusters. Computations of WD isochrones require, in addition to a grid of WD models covering the relevant mass range, an IFMR, plus evolutionary timescales of the WD progenitors.

Figure 9 shows three sets of isochrones in the L–T_{eff} plane, with ages equal to 1, 5, and 10 Gyr, for our H-atmosphere (solid lines) and He-atmosphere (dotted line) cooling models including phase separation upon crystallization. We also include (dashed lines) isochrones for the S00 models (with hydrogen atmospheres) again including phase separation. All displayed isochrones have been computed using the IFMR by Salaris et al. (2009)[7] and progenitor lifetimes from BaSTI models (with convective core overshooting during the main sequence) for a metallicity $Z = 0.0198$. As discussed before, the choice of the progenitor metallicity and IFMR has a small impact on the CO stratification and cooling times of models with fixed M_{WD}, and one can couple our sets of WD models to different choices for the IFMR and progenitor metallicity.

As is well known (see, e.g., Salaris 2009 for a review), the age indicator is the faint end of the isochrones. The more massive WDs formed from higher-mass and shorter-lived progenitors

---

[7] We employed the linear analytic fit, extrapolated—when necessary—down to the smallest value of the progenitor mass appropriate for the chosen isochrone age. The upper value of the initial mass is set by the minimum stellar mass igniting carbon core burning, as derived from the BaSTI calculations.
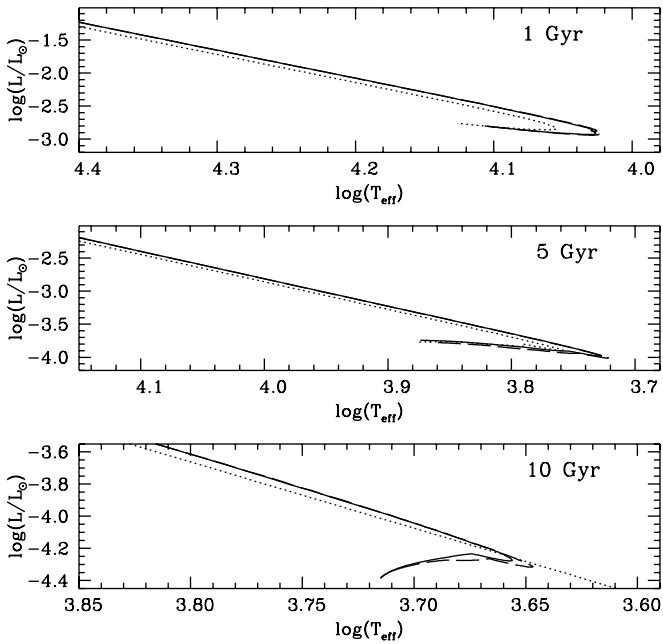
Figure 9. Three sets of WD isochrones (including phase separation) for each of the labeled ages. Solid lines denote H-atmosphere isochrones, dotted lines He-atmosphere isochrones, and dashed lines isochrones calculated from the S00 WD models (see the text for details). Note the change of scale between panels.

Figure 10. Same isochrones of Figure 9, this time in the ACS F555W−(F555W−F814W) plane. The line styles are as in Figure 9.

pile up at the bottom of the cooling sequence, where they produce the characteristic turn to the blue, i.e., a turn toward lower radii (Isern et al. 1998). An age increase makes the bottom end of the isochrones fainter, because of the longer cooling times.

A qualitative analysis of Figure 9 shows that H-atmosphere WD isochrones computed from S00 models have only slightly fainter termination at ages of 5 and 10 Gyr, compared to our results. On the other hand, our He-atmosphere WD isochrones have a brighter faint end than the H-atmosphere counterpart at ages of 1 and 5 Gyr, while at 10 Gyr they reach much lower luminosities. Given that progenitor ages and IFMR are the same for all three sets of isochrones, this behavior is due to differences in the cooling times of the underlying WD models. As we have seen before, for luminosities down to $\log(L/L_\odot) \approx -4$, He-atmosphere models predict a slower cooling, hence the brighter termination of the WD isochrones for 1 and 5 Gyr.

Another interesting result of the comparisons in Figure 9 is the general shift of He-atmosphere isochrones toward lower radii, very evident when the luminosity is above $\log(L/L_\odot) \approx -4$. There are two reasons for this behavior. The first one is related to the fact that along a WD isochrone of age t, the sum of the WD cooling age and the corresponding progenitor lifetime has to be equal to t. Above $\log(L/L_\odot) \approx -4$ He-atmosphere models with a given M_{WD} have longer cooling times and, as a consequence, a given luminosity along an isochrone has to be populated by a larger WD mass (smaller radius) in the non-DA case, because its earlier formation (lower progenitor lifetimes) compensates for the longer cooling times. An additional contribution to this difference stems from the fact that, as shown in Figure 8, He-atmosphere WD models of a given M_{WD} have (at fixed T_{eff}) smaller radii than the H-atmosphere counterpart.

Figure 10 displays the same sets of isochrones, this time in an observational plane, i.e., employing the absolute magnitudes in the F555W and F814W filters of the Advanced Camera for
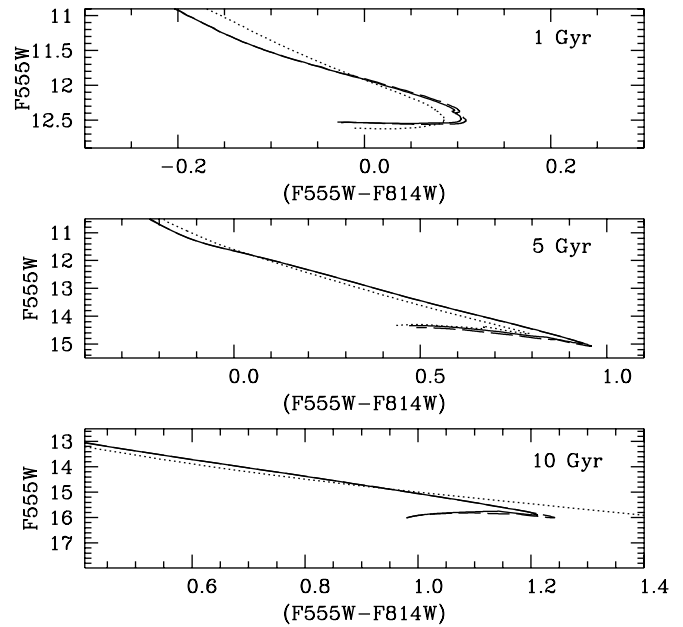
Surveys (ACS) camera on board the *Hubble Space Telescope* (*HST*). The reference set of bolometric corrections (used for Figure 10) that we apply to all our WD models and isochrones is the same employed in Bedin et al. (2005), i.e., an extension of the results of Bergeron et al. (1995—see, e.g., Section 3.1 in Holberg & Bergeron 2006). One can notice how the different behavior of the bolometric corrections for H and He atmospheres alters the relative location of the corresponding isochrones, compared to Figure 9. Despite the longer cooling times of He-atmosphere WD models, the termination of the isochrone at 1 Gyr is now fainter than the H-atmosphere one. The differences in the bolometric corrections and colors of our H- and He-atmosphere cooling tracks can be appreciated even better in Figure 11 that displays a color–color diagram for the 0.61 and 1.0 $M_\odot$ tracks with both H (solid lines) and He atmospheres (dashed lines). The He-atmosphere colors increase steadily along the evolution, whereas the (F555W−F814W) color of the H-atmosphere models displays a more complex behavior, with a marked decrease at low effective temperatures, due to the blocking effect in the infrared of the H_2 collision-induced absorption (e.g., H99; Saumon & Jacobson 1999). The onset of this turn to the blue of (F555W−F814W) is at ages above 14 Gyr, but is attained earlier (and the turn to the blue more pronounced) in near-infrared colors. In the future, we will update the adopted set of bolometric corrections by calculating theoretical spectra from the new atmospheres employed for the boundary conditions of our WD models. In the new pure H model atmospheres, the updated calculation of the Ly_α opacity causes the removal of flux from short wavelengths and its redistribution to longer wavelengths (Kowalski 2007), compared to previous calculations. As for the new pure He model atmospheres, a stronger ionization makes the He-ff opacity dominant over Rayleigh scattering at all wavelengths (Kowalski et al. 2007), and the spectral energy distribution is closer to a blackbody compared to Bergeron et al. (1995) results. Some preliminary estimates for gravities typical of a 0.6 $M_\odot$ WD model show that color transformations from the new model atmospheres will produce redder colors for both H and He atmospheres.
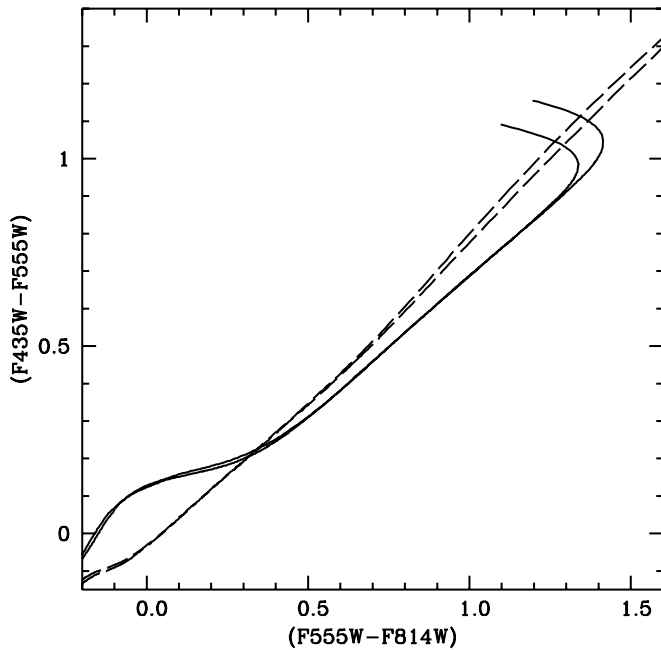
Figure 11. (F435W−F555W) vs. (F555W−F814W) diagram in the ACS photometric system, for the 0.61 and 1.0$M_\odot$ cooling tracks (including phase separation) with H- (solid lines) and He-atmospheres (dashed lines).

Table 1
Correspondence Between the LF Cutoff Ages for the Following Three Sets of Models (See the Text for Details)

H-atm.	He-atm.	H-atm. S00
1.0 Gyr	0.9 Gyr	1.0 Gyr
5.0 Gyr	5.5 Gyr	4.7 Gyr
10.0 Gyr	6.5 Gyr	9.7 Gyr

One can derive a quantitative estimate of the age differences obtained when the three sets of isochrones in Figure 10 are applied to real data, in the following way. We have first calculated the LFs in the F606W passband for the three H-atmosphere isochrones in Figure 10, assuming a Salpeter mass function (MF) for the progenitors. For the three reference ages of 1, 5, and 10 Gyr, we have determined the magnitude of the LF cutoff, that corresponds to the faint end of the isochrones. These three LFs are considered to be the "observed" LFs of three populations of known ages. We have then computed several isochrones and LFs from both our He-atmosphere calculations, and from the older S00 models, and determined what ages are necessary to match the position of the LF cutoffs of the three reference "observed" populations.

The results, reported in Table 1, show that S00 models provide ages very similar to our new H-atmosphere cooling models, across the whole range explored by this test. This implies that all WD ages in the series of papers by Bedin and collaborators (e.g., Bedin et al. 2010, and references therein) obtained using S00 models (and BaSTI progenitor lifetimes) are basically confirmed by our new calculations. Also the derivation of the semiempirical IFMR by Salaris et al. (2009), which makes use of H-atmosphere WD ages estimated from S00 models, is basically unaffected. On the other hand, He-atmosphere isochrones give, as well known, much younger ages for the oldest population, but 10% older ages at 5 Gyr, and 10% younger ages at 1 Gyr.
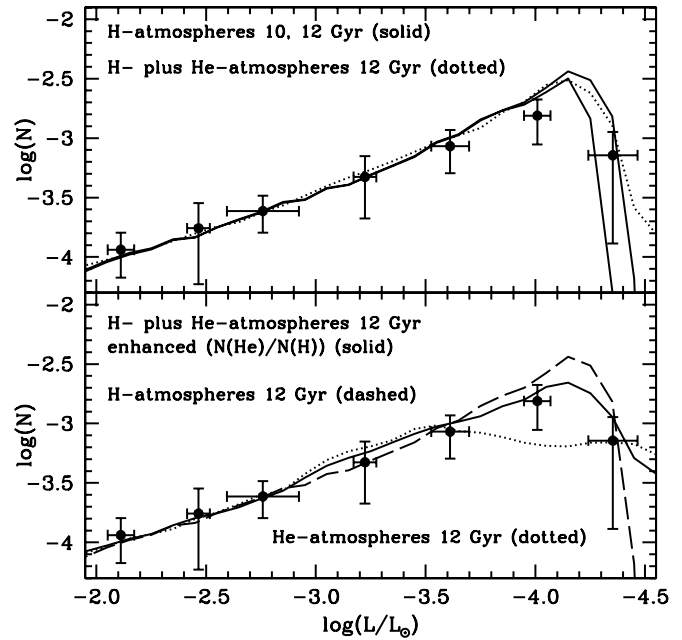

Figure 12. Upper panel: observed LF for WDs in the solar neighborhood from Catalan et al. (2008) compared, respectively, to H-atmosphere theoretical LFs and a mixed H- and He-atmosphere LF with a number ratio (N(He)/N(H)) equal to the observed mean value at $T_{\rm eff} = 14,000$ K (see the text for details). Lower panel: the observed LF is compared to, respectively, H- and He-atmosphere LFs, and an LF with an enhanced (N(He)/N(H)) ratio (see the text for details). All theoretical LFs are computed from WD models including the effect of phase separation upon crystallization.

3.1. The WD Population in the Solar Neighborhood

We close this section with an example of application of our models to real data. Figure 12 displays an observational LF of WDs in the solar neighborhood, from Catalan et al. (2008, compiled from several sources) compared to several theoretical LFs. More in detail, we calculated LFs from both our H-atmosphere (with and without phase separation) and He-atmosphere (only the ones with phase separation included) models, considering progenitors with metallicity $Z = 0.0198$ (including main sequence convective core overshooting) and a Salpeter MF, plus IFMR from Salaris et al. (2009), and a constant star formation rate starting t Gyr ago. All theoretical LFs are normalized to the observed star counts at $\log(L/L_\odot) = -2.76$. Matching the position of the cutoff of this empirical LF with H-atmosphere models provides an age $t \sim 12$ Gyr for the onset of star formation when phase separation is included, and $\sim$11 Gyr when phase separation is neglected. The formal error bar on t is set by the horizontal error bar on the last point of the empirical LF, and is of the order of ± 2 Gyr. We have also considered the effect of He-atmosphere WDs in the theoretical LF, by computing first an LF assuming the same parameters as for the H-atmosphere case. As a second step, we have built a composite LF adding up the star counts in the H- and H-atmosphere LFs, whereby the number ratio (N(He)/N(H)) of He- to H-atmosphere WDs has been set to reproduce the observed mean value (N(He)/N(H)) = 0.268 at $T_{\rm eff} = 14,000$ K (Tremblay & Bergeron 2008). This composite LF has been then normalized to match the observed WD counts at $\log(L/L_\odot) = -2.76$. Figure 12 shows that our composite LF displays, at a given t, a sharp drop in star counts at approximately the same luminosity of the cutoff in the H-atmosphere LF, with a spread of objects distributed toward lower luminosities, due to

the faster cooling times of the oldest He-atmosphere objects. As a further test, we have computed a 12 Gyr LF with both H- and He-atmosphere objects—constructed as described before—with a constant star formation rate and a progenitor metallicity equal to $Z = 0.004$ for WD ages t between 12 and 8 Gyr, $Z = 0.008$ when t is between 8 and 4 Gyr, and up to $Z = 0.0198$ for ages below 4 Gyr. The result is barely different from the case of constant progenitor metallicity.

As mentioned before, in the composite LF with both H- and He-atmosphere objects we have normalized the ratio (N(He)/N(H)) by matching the observed mean value at $T_{\rm eff} = 14,000$ K. Tremblay & Bergeron (2008) investigation shows that the observed (N(He)/N(H)) ratio increases up to ∼0.45 when $T_{\rm eff} < 10,000$ K, and the authors conclude that the only physical mechanism able to account for this increase is the convective mixing of the thin hydrogen layers with the underlying helium envelope. Here, we study how (N(He)/N(H)) changes in our modeling of the local WDs, due exclusively to the different cooling times of H- and He-atmosphere models. We are assuming in this analysis that both types of WDs are born independently with the same IFMR, from progenitors formed with a constant formation rate and a Salpeter MF. Our choice of thick H layers prevents any mixing of the H-rich envelope with the underlying, much more massive He layers. Figure 12 displays two theoretical LFs, one with only H-atmosphere objects, and one with only He-atmosphere WDs, both normalized to the observed star counts at $\log(L/L_\odot) = -2.76$. In this way, just by comparing the two LFs, we have a first visual impression of the intrinsic, appreciable variation of the ratio (N(He)/N(H)) with luminosity, hence $T_{\rm eff}$, due to the different cooling timescales of the models. It is immediately clear that (N(He)/N(H)) does not stay constant along the LF; there is a luminosity interval, between $\log(L/L_\odot) \sim -2.85$ and ∼−3.5, where (N(He)/N(H)) increases, before dropping fast at lower luminosities, and eventually increasing again around the cutoff luminosity, due to the disappearance of H-atmosphere objects.

Figure 13 displays the predicted (N(He)/N(H)) number ratio (solid line) this time as a function of $T_{\rm eff}$ that can be compared directly with the empirical result by Tremblay & Bergeron (2008). In this figure, the theoretical values have been determined by means of a Monte Carlo simulation that uses as input the constant star formation rate, constant $Z = 0.0198$ progenitor metallicity, the same IFMR and MF employed in the calculation of the LF, and a Galactic disk age of 12 Gyr. We calculate two synthetic samples of H- and He-atmosphere objects, respectively. For each synthetic WD produced in our simulation, we perturbed the $T_{\rm eff}$ by a 1σ Gaussian error equal to 5% of the actual value of $T_{\rm eff}$, to mimic the typical errors in the empirical $T_{\rm eff}$ by Tremblay & Bergeron (2008). We have then grouped the resulting sample (over 100,000 H- and He-atmosphere objects, to avoid statistical number fluctuations in the synthetic sample) in the same $T_{\rm eff}$ bins chosen by Tremblay & Bergeron (2008). The (N(He)/N(H)) values have been first normalized to reproduce the observed mean value at $T_{\rm eff} = 14,000 \pm 1000$ K, and then compared with the empirical data.

One can notice that (N(He)/N(H)) stays roughly constant between $T_{\rm eff}$ ∼14,000 K and ∼10,000 K, as observed. Below this temperature the ratio increases at first, following the observations. This is at odds with the interpretation by Tremblay & Bergeron (2008); according to our modeling of the solar neighborhood WDs, this increase is simply due to the different cooling times of H- and He-atmosphere WDs in this $T_{\rm eff}$ range. However, the theoretical value drops below the data when $T_{\rm eff} \sim 8000$ K.
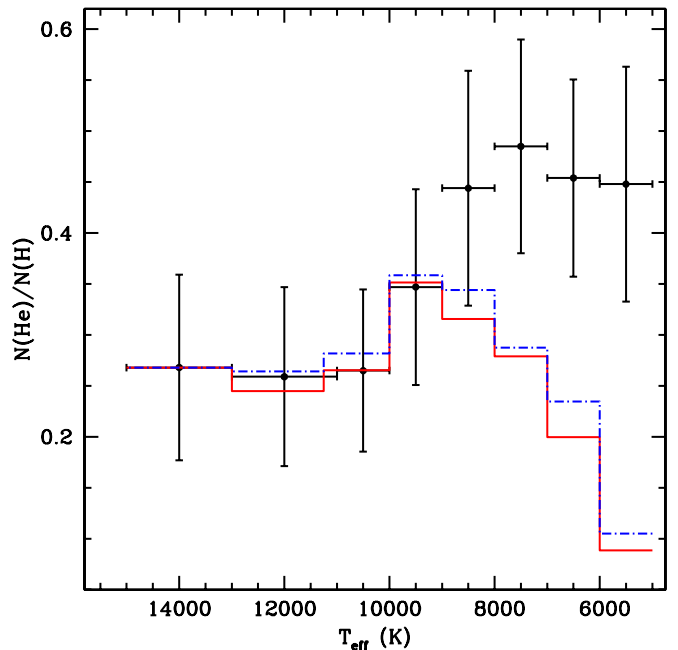

Figure 13. (N(He)/N(H)) number ratio as a function of $T_{\rm eff}$. Points with error bars represent the data by Tremblay & Bergeron (2008). The solid line displays the predictions from the 12 Gyr theoretical LFs with both H- and He-atmosphere objects, shown in Figure 12. The (N(He)/N(H)) ratio is set to the observed mean value at $T_{\rm eff} = 14,000$ K. The dash-dotted lines show the predicted (N(He)/N(H)) ratio for our simulation with progenitor metallicity varying with age.
(A color version of this figure is available in the online journal.)

We have also determined the evolution of (N(He)/N(H)) with $T_{\rm eff}$ in our simulation with metallicity increasing with decreasing WD age, and the result is not changed significantly. The difference between observed and predicted ratio gets larger than the 2σ errors for the two coolest bins centered at 6500 K and 5500 K, respectively. The coolest temperature bin for the observed sample corresponds approximately to the luminosity of the peaks of the theoretical LFs displayed in the top panel of Figure 12 ($\log(L/L_\odot) \sim -4.2$). For heuristic purposes it is important to mention that the theoretical (N(He)/N(H)) ratio reaches a minimum value of ∼0.06 at $T_{\rm eff} \sim 5000$ K, beyond the lowest temperature limit of Tremblay & Bergeron (2008) data, before starting to increase. At $T_{\rm eff} \sim 4300$ K the predicted value of (N(He)/N(H)) is again equal to 0.268, and increases steadily at lower temperatures, so that He-atmosphere objects are expected to dominate the population of the fainter bin of the observed LF, as is also clear from the lower panel of Figure 12.

The comparison in Figure 13 shows that it still seems necessary to invoke the transformation of some H-atmosphere WDs into He-atmosphere objects to reproduce the spectroscopic observations at low $T_{\rm eff}$, in the assumption of a constant progenitor formation rate and an (N(He)/N(H)) ratio at the start of the WD phase that is constant with time. The onset of this spectral transformation and the quantitative details are however different from the conclusions by Tremblay & Bergeron (2008), who assumed a constant baseline value of (N(He)/N(H)), instead of an intrinsic variation with $T_{\rm eff}$ due to WD evolutionary effects. The temperature where the theoretical ratio drops significantly below the data constrains the thickness of the H layers in the objects that undergo the spectral transformation. The lower the temperature, the thicker (in mass) the H layers. From the results in Figure 1 of Tremblay & Bergeron (2008) and our own models, for the case of a 0.6 $M_\odot$ WD, H–He mixing at $T_{\rm eff} = 7000$ K implies $\log(q({\rm H})) \sim -8.5$, while mixing at

$T_{\rm eff} = 6000$ K corresponds to $\log(q(H)) \sim -7.0$. Assuming a constant observed mean value $(N({\rm He})/N({\rm H})) = 0.45$ when $T_{\rm eff}$ is below 8000 K, one needs a fraction of H-atmosphere objects undergoing spectral transformation that increases with decreasing $T_{\rm eff}$, reaching a maximum of $\sim 24\%$ at the lowest temperature bin sampled by Tremblay & Bergeron (2008). This is consistent with a broad range of H-layer thickness in solar neighborhood H-atmosphere WDs, progressively thicker H envelopes being mixed at increasingly lower $T_{\rm eff}$.

Finally, to gain a very approximate idea of the impact of this spectral transformation on the theoretical LF, we display in Figure 12 also the case of a mixed H- and He-atmosphere population, where $(N({\rm He})/N({\rm H}))$ has been normalized appropriately to reach the value $(N({\rm He})/N({\rm H})) = 0.45$ at $\log(L/L_\odot) = -4.2$ (i.e., it is about 4 times larger at $T_{\rm eff} \sim 14{,}000$ K than our reference case displayed in the top panel of the same figure). The LF cutoff is less sharp, the mean age of the onset of star formation in the solar neighborhood is decreased by ~ 1 Gyr.

4. SUMMARY

We have expanded our BaSTI stellar evolution archive by including new, updated WD cooling models, computed using the CO stratification obtained from BaSTI AGB progenitor calculations. Improvements with respect to the S00 set of WD models concern the CO chemical profiles, that have been obtained employing an updated estimate of the $^{12}{\rm C}(\alpha, \gamma)^{16}{\rm O}$ reaction rate, and the inclusion of a full set of He-atmosphere WD models, computed with appropriate boundary conditions from non-gray model atmospheres. The reference set of WD models that will be made public at the BaSTI Web site makes use of the CO stratification at the first thermal pulse from progenitor models calculated with initial metal mass fraction $Z = 0.0198$, and the inclusion of convective core overshooting during the main sequence. To assess how sensitive the models are to these assumptions, we have tested the effect of uncertainties on the recent determination of the $^{12}{\rm C}(\alpha, \gamma)^{16}{\rm O}$ reaction rate employed in the progenitor models, the inclusion/exclusion of core convective overshooting during the main sequence, different approaches for quenching the breathing pulses at the end of core He-burning, a variation of the metallicity of the progenitor, a variation of the number of pulses experienced by the progenitor models.

The results of this analysis indicate that the uncertainty on the $^{12}{\rm C}(\alpha, \gamma)^{16}{\rm O}$ reaction rate and the numerical approach used for inhibiting the breathing pulses have on the whole the largest impact on the WD cooling times, of about 7% at most—or of about 3% when the effect of phase separation upon crystallization is neglected. The progenitor metallicity, convective core overshooting during the main sequence phase, and the number of pulses before the WD formation have overall a smaller effect.

We have discussed quantitatively differences in the mass–radius relationships and cooling speed of H- and He-atmosphere cooling models. The radii of the He-atmosphere models of a given mass are systematically lower than their H-atmosphere counterparts. Differences range between $\sim 9\%$ and $\sim 3\%$ increasing with decreasing $M_{\rm WD}$ and/or increasing temperature. He-atmosphere models show typically longer cooling times down to $\log(L/L_\odot) \approx -4$, before starting to cool down much faster at lower luminosities. We have also estimated the differences between ages of star clusters obtained employing our new H- and He-atmosphere WD models, as well as the S00 H-atmosphere WD calculations. Ages derived from S00

H-atmosphere models show only relatively small differences when compared to our new calculations.

As an example of application of our new set of models to real data, we have estimated an age of ~ 12 Gyr for the onset of star formation in the solar neighborhood, by fitting the local WD LF compiled by Catalan et al. (2008). We have also studied the variation of the number ratio $(N({\rm He})/N({\rm H}))$ with $T_{\rm eff}$, predicted by our simulation of the local WDs. Due to the different cooling times of H- and He-atmosphere models, we show how this ratio changes with $T_{\rm eff}$, increasing below $T_{\rm eff} \sim 10{,}000$ K, as observed. However, at least with our assumptions about the formation of the local WDs—a constant progenitor formation rate and an $(N({\rm He})/N({\rm H}))$ ratio at the onset of the WD phase that is constant with time—the predicted ratio drops well below the observed value when $T_{\rm eff}$ is lower than 7000–8000 K. This result can be explained in terms of the spectral transformation of a fraction of H-atmosphere objects that increases with decreasing $T_{\rm eff}$ below 7000–8000 K, reaching a maximum of $\sim 24\%$ at the lowest temperatures sampled by the observational data. As a consequence, one needs a broad range of H-layer thickness in solar neighborhood H-atmosphere WDs to explain these spectral changes, thicker envelopes being mixed with the underlying more massive He layers at increasingly lower $T_{\rm eff}$.

All cooling tracks and the reference chemical stratifications will be made publicly available at the official BaSTI Web site (http://www.oa-teramo.inaf.it/BASTI). In addition, we provide WD isochrones for ages between 200 Myr and 14 Gyr for both H- and He-atmosphere objects (with and without the inclusion of phase separation) using as a reference the IFMR by Salaris et al. (2009) and the progenitor lifetimes from BaSTI models including convective core overshooting on the main sequence. The isochrones will be available for progenitors with both scaled solar and α-enhanced mixtures, and 11 values of the metal fraction Z, ranging from $Z = 0.0001$ to $Z = 0.04$. For both cooling tracks and isochrones we provide magnitudes in the UBVRIJHK and *HST* ACS photometric systems.

REFERENCES

Alexander, D. R., Brocato, E., Cassisi, S., Castellani, V., Ciacio, F., & degl'Innocenti, S. 1997, A&A, 317, 90

Althaus, L. G., & Benvenuto, O. G. 1998, MNRAS, 296, 206

Althaus, L. G., Panei, J. A., Romero, A. D., Rohrmann, R. D., Corsico, A. H., Garciá-Berro, E., & Miller Bertolami, M. M. 2009, A&A, 502, 207

Bedin, L. R., King, I. R., Anderson, J., Piotto, G., Salaris, M., Cassisi, S., & Serenelli, A. 2008, ApJ, 678, 1279

Bedin, L. R., Salaris, M., King, I. R., Piotto, G., Anderson, J., & Cassisi, S. 2010, ApJ, 708, L32

Bedin, L. R., Salaris, M., Piotto, G., Anderson, J., King, I. R., & Cassisi, S. 2009, ApJ, 697, 965

Bedin, L. R., Salaris, M., Piotto, G., King, I. R., Anderson, J., Cassisi, S., & Momany, Y. 2005, ApJ, 624, L45

Bergeron, P., Saffer, R. A., & Liebert, J. 1992, ApJ, 394, 228

Bergeron, P., Wesemael, F., & Beauchamp, A. 1995, PASP, 107, 1047

Caputo, F., Castellani, V., Chieffi, A., Pulone, L., & Tornambé, A. 1989, ApJ, 340, 241

Cassisi, S., Castellani, V., Degl'Innocenti, S., Piotto, G., & Salaris, M. 2001, A&A, 366, 578

Cassisi, S., Salaris, M., & Irwin, A. W. 2003, ApJ, 588, 862

Castellani, V., Chieffi, A., Pulone, L., & Tornambé, A. 1985, ApJ, 296, 204

Catalan, S., Isern, J., Garcia-Berro, E., & Ribas, I. 2008, MNRAS, 387, 1693

Caughlan, G. R., Fowler, W. A., Harris, M. J., & Zimmermann, B. A. 1985, At. Data Nucl. Data Tables, 32, 197

Cordier, D., Pietrinferni, A., Cassisi, S., & Salaris, M. 2007, AJ, 133, 468

Dorman, B., & Rood, R. T. 1993, ApJ, 409, 387

Dufour, M., & Descouvemont, P. 2008, Phys. Rev. C, 78, 015808

Fontaine, G., Brassard, P., & Bergeron, P. 2001, PASP, 113, 409

Garcia-Berro, E., Hernanz, M., Mochkovitch, R., & Isern, J. 1988a, A&A, 193, 141

Garcia-Berro, E., Hernanz, M., Mochkovitch, R., & Isern, J. 1988b, Nature, 333, 642

Hansen, B. M. S. 1999, ApJ, 520, 680 (H99)

Hansen, B. M. S., et al. 2004, ApJS, 155, 551

Hansen, B. M. S., et al. 2007, ApJ, 671, 380

Holberg, J. B., & Bergeron, P. 2006, AJ, 132, 1221

Iben, I. Jr., & MacDonald, J. 1986, ApJ, 301, 164

Iglesias, C. A., & Rogers, F. J. 1993, ApJ, 412, 752

Isern, J., Garcia-Berro, E., Hernanz, M., & Chabrier, G. 2000, ApJ, 528, 397

Isern, J., Garcia-Berro, E., Hernanz, M., Mochkovitch, R., & Torres, S. 1998, ApJ, 503, 239

Katsuma, M. 2008, Phys. Rev. C, 78, 034606

Koester, D. 2009, A&A, 498, 517

Kowalski, P. M. 2006a, ApJ, 641, 488

Kowalski, P. M. 2006b, ApJ, 651, 1120

Kowalski, P. M. 2007, A&A, 474, 491

Kowalski, P. M., Mazevet, S., Saumon, D., & Challacombe, M. 2007, Phys. Rev. B, 76, 075112

Kowalski, P. M., & Saumon, D. 2004, ApJ, 607, 970

Kowalski, P. M., & Saumon, D. 2006, ApJ, 651, L137

Kunz, R., Fey, M., Jaeger, M., Mayer, A., Hammer, J. W., Staudt, G., Harissopulos, S., & Paradellis, T. 2002, ApJ, 567, 643

Mazzitelli, I., & D'Antona, F. 1987, in IAU Coll. 95, The 2nd Conf. Faint Blue Stars, ed. A. G. D. Philip, S. Hayes, & J. Liebert (Schenectady, NY: Davis), 351

Mochkovitch, R. 1983, A&A, 122, 212

Montgomery, M. H., Klumpe, E. W., Winget, D. E., & Wood, M. A. 1999, ApJ, 525, 482

Oswalt, T. D., Smith, J. A., Wood, M. A., & Hintzen, P. M. 1996, Nature, 382, 692

Percival, S. M., Salaris, M., Cassisi, S., & Pietrinferni, A. 2009, ApJ, 690, 427

Pietrinferni, A., Cassisi, S., Salaris, M., & Castelli, F. 2004, ApJ, 612, 168

Pietrinferni, A., Cassisi, S., Salaris, M., & Castelli, F. 2006, ApJ, 642, 797

Pietrinferni, A., Cassisi, S., Salaris, M., Percival, S., & Ferguson, J. W. 2009, ApJ, 697, 275

Prada-Moroni, P. G., & Straniero, O. 2002, ApJ, 581, 585

Richer, H. B., Fahlman, G. G., Rosvick, J., & Ibata, R. 1998, ApJ, 504, L91

Salaris, M. 2009, in IAU Symp. 258, The Ages of Stars, ed. E. E. Mamajek, D. R. Soderblom, & R. F. G. Wyse (Dordrecht: Kluwer), 287

Salaris, M., Dominguez, I., García-Berro, E., Hernanz, M., Isern, J., & Mochkovitch, R. 1997, ApJ, 486, 413

Salaris, M., García-Berro, E., Hernanz, M., Isern, J., & Saumon, D. 2000, ApJ, 544, 1036 (S00)

Salaris, M., Serenelli, A., Weiss, A., & Miller Bertolami, M. 2009, ApJ, 692, 1013

Saumon, D., & Jacobson, S. B. 1999, ApJ, 511, L107

Segretain, L., Chabrier, G., Hernanz, M., Garca-Berro, E., Isern, J., & Mochkovitch, R. 1994, ApJ, 434, 641

Serenelli, A. M., Althaus, L. G., Rohrmann, R. D., & Benvenuto, O. G. 2002, MNRAS, 337, 1091

Stevenson, D. J. 1977, PASA, 3, 167

Straniero, O., Domínguez, I., Imbriani, G., & Piersanti, L. 2003, ApJ, 583, 878

Tremblay, P.-E., & Bergeron, P. 2008, ApJ, 672, 1144

von Hippel, T. 2005, ApJ, 622, 565

Winget, D. E., et al. 1987, ApJ, 315, L77

Wood, M. A. 1992, ApJ, 386, 539